Supporting Information:

Layer dependent Interfacial Transport and Optoelectrical properties of MoS_2 on Ultra-flat metals

Hao Lee[1], S. Deshmukh[2], Jing Wen[3,4], V.Z. Costa[1], J. S. Schuder[5], M. Sanchez[5], A. Ichimura[5], Eric Pop[2,6,7], Bin Wang[3], and A. K. M. Newaz[1,*]

[1]Department of Physics and Astronomy, San Francisco State University, San Francisco, California 94132, USA

[2]Department of Electrical Engineering, Stanford University, Stanford, California 94305, USA

[3]School of Chemical, Biological and Materials Engineering, University of Oklahoma, Norman, Oklahoma 73019, United States

[4]Key Laboratory for Photonic and Electronic Bandgap Materials, Ministry of Education, School of Physics and Electronic Engineering, Harbin Normal University, Harbin 150025, P. R. China

[5]Department of Chemistry and Biochemistry, San Francisco State University, San Francisco, California 94132, USA

[6]Department of Materials Science and Engineering, Stanford University, Stanford, California 94305, USA

[7]Precourt Institute for Energy, Stanford University, Stanford, California 94305, USA

[*]Email:akmnewaz@gmail.com

S1. TE-Au surface roughness

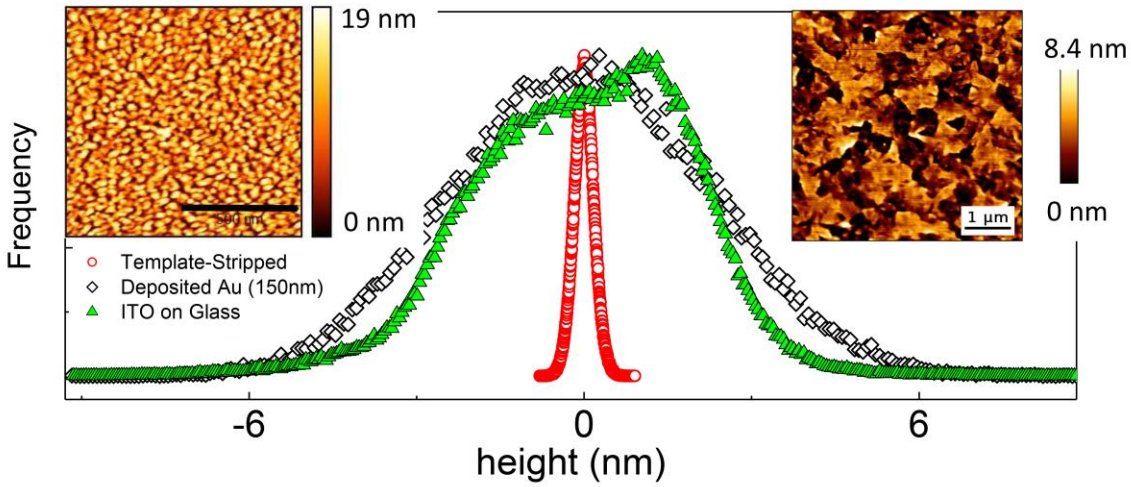

Figure S1: Surface roughness of thermally evaporated Au substrate and commercially available ITO on a glass substrate (Delta Technologies). Main panel: histogram of the height distribution (surface roughness measured by AFM) of the template-stripped Au substrate (red circle), as thermally evaporated Au (black square) substrate of thickness ~150 nm and commercial ITO on a glass substrate (green triangle). The root mean squared (RMS) value of the surface roughness measured was ~ 0.18 nm for template-stripped Au and ~1.8 nm for as-deposited Au substrate and ~1.9 nm for ITO on a glass substrate. Inset-left: tapping mode AFM image of the thermally evaporated Au surface. Inset-right: tapping mode AFM image ITO coated glass substrate. A Gaussian fit to the height data provides full width at half maxima (FWHM) ~ 0.3 nm for the template-stripped Au, ~ 5 nm for as-deposited Au and ~ 4 nm for the ITO substrate.

S2. Layer number determination by Raman Spectroscopy.

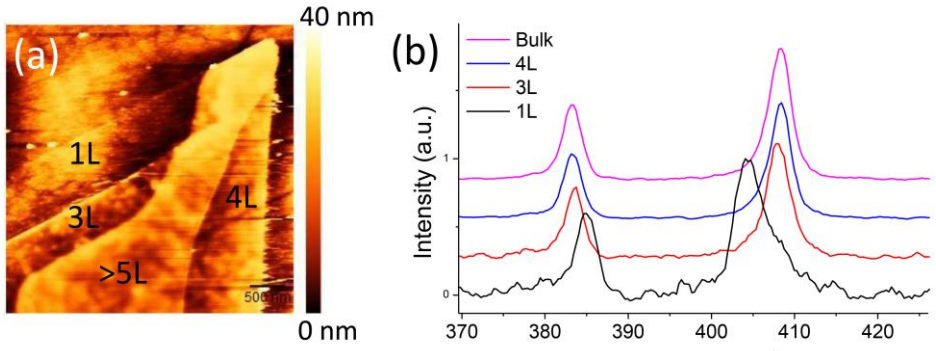

Figure S2: Raman based layer number determination. (a) AFM height profile of few layer MoS_2 on a ultra-flat ITO. The scale bar is 500 nm (b) Raman spectroscopy data for different layers. Here we define bulk as 5L or more layers MoS_2.

S3. Electronic transport between metallic AFM tip and bare Au substrate

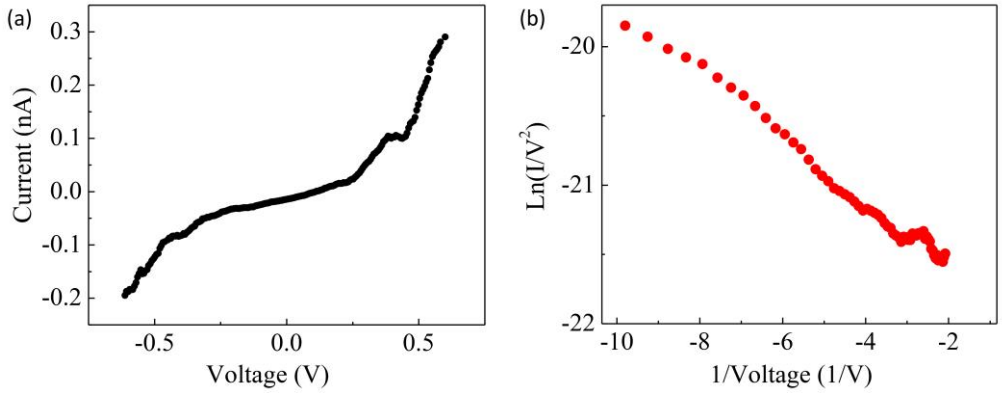

Figure S3: I-V curve for a bare template-stripped Au substrate. (a) Measured I-V curve. (b) $\ln(\frac{I}{V^2}) - 1/V$ plot for the data shown in (a) . The linear behavior suggests a tunneling current between the AFM tip and bare Au substrate.

S4. Electronic transport between metallic AFM tip and bare Au substrate after exfoliation

We observed that the current is vanishingly small outside the MoS_2 sample as in Fig.2 and Fig.3 main text. To determine the reason, we conducted a control CAFM measurements of template stripped Au-substrate before and after the micro-exfoliation. We have observed that the conducting current drops by ~4 orders of magnitude after exfoliating the samples as shown in Figure S4. This suggests that the micro-exfoliation leaves residues and make the metal surfaces non-conducting.

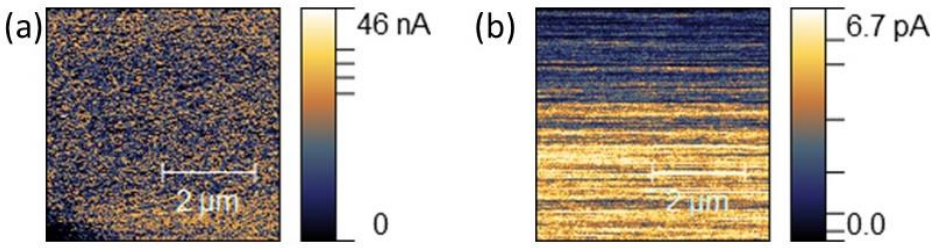

Figure S4: CAFM measurement of a template stripped-Au substrate before exfoliation (a) and after exfoliation (b). Note that the current drops by ~4 orders due to the exfoliation. The measurements were taken at 0.7 V for both cases.

S5: *I-V* analysis in the forward bias regime and the negative bias regime

To determine the electronic transport mechanism governing the *I-V* curve, we prepared 1L-MoS_2 and 2L-MoS_2 sample on template-stripped Au substrate. We measured I-V curve using the voltage spectroscopy mode (also known as cyclic voltammetry mode) of the CAFM measurements provided by the AFM manufacturer (JPK). The experimentally

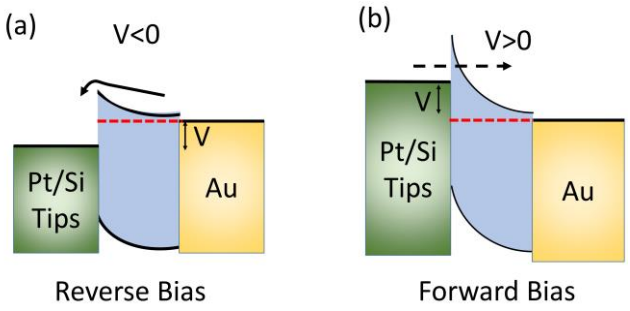

Figure S5: (a) Schematic band diagram of a thin MoS_2 and Pt-Silicide tip junction under reverse bias. (b) Schematic band diagram of a thin MoS_2 and Pt-Silicide tip junction under forward bias.

measured *I-V* curves for 1L-MoS_2 and 2L-MoS_2 are presented in Fig.S6 (a-b). We observed that the *I-V* curves in the forward bias regime and reverse bias regime are not symmetric, which suggests that the different transport mechanisms are determining the current through our vertical structures. We present schematic band structures of Pt-Silicide/MoS_2/Au in Fig.S5. When a metal tip is brought into contact with MoS_2, a Schottky barrier forms, whose height depends on the work function of Pt-Silicide tip and the electron affinity of MoS_2.[1-3]

In the forward bias regime (Fig.S5-b), high barrier height suppresses the thermionic emission and the barrier thickness is reduced with higher applied bias, which results in a tunneling current. This forward current can be modeled by FN tunneling model, which has been widely used to explain the tunneling of an electron between two metals separated by an insulator or semiconductor.[3-6] The tunneling current through a thin semiconductor is given by

$$I(V) = \frac{A_e q^3 m V^2}{8\pi h \Phi_B d^2 m^*} \exp\left(-\frac{8\pi\sqrt{2m^*}\Phi_B^{3/2} d}{3hqV}\right) \quad (1)$$

where A_e is the effective contact area, h is Planck's constant, q is the electron charge, d is the thickness of the barrier, Φ_B is the barrier height, m is the electron mass, and m^* is the electron effective mass inside the semiconductor. We used $\frac{m^*}{m} \sim 0.35$ and 0.53 for monolayer MoS_2 and bulk MoS_2 (>1L), respectively.[3] Our fitting for 1L-MoS_2 and 2L-MoS2 are shown in Fig.S6(a-b), which shows an excellent agreement. The above equation (1) suggests that FN tunneling results a linear $\ln\frac{I}{V^2}$ versus $1/V$ plot. Indeed, we observed that $\ln\frac{I}{V^2}$ varies linearly as a function of $1/V$, as shown in the Fig. S6(b) and Fig.6(e) for 1L-MoS_2 and 2L-MoS_2, respectively. But, in the reverse bias regime, we observed that $\ln\frac{I}{V^2}$ varies non-linearly as a function of 1/V as shown in Fig.S6(c) and Fig.S6(f) for 1L-MoS_2 and 2L-MoS_2, respectively. Hence *I-V* behavior in the forward and reverse bias regime confirms that the current in the forward bias is determined by the FN tunneling and the current in the reverse bias is not due to FN tunneling.

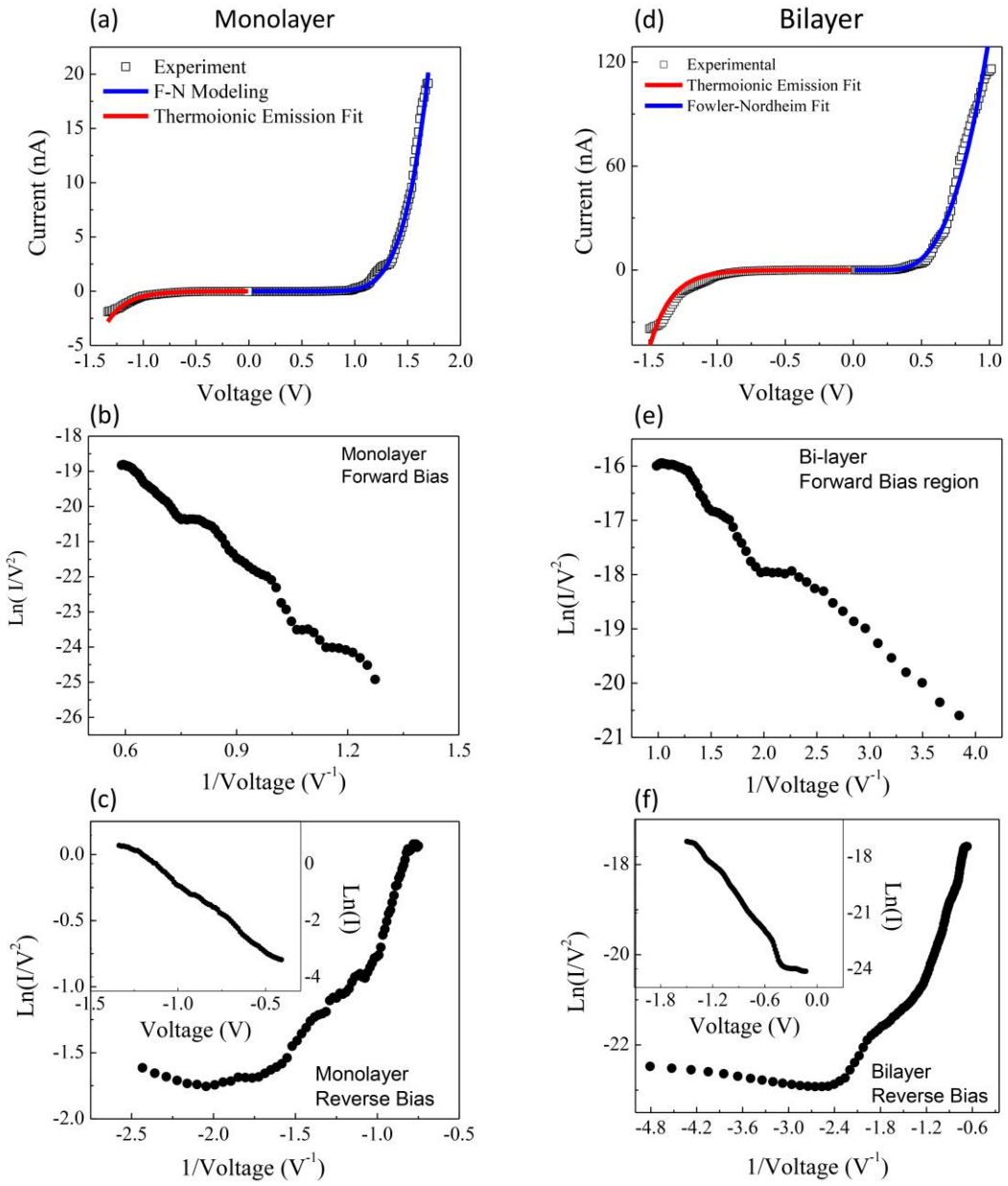

Figure S6: Current-voltage (I-V) measurement and the analysis of a 1L-MoS_2 (Left row) and 2L-MoS_2 (right row). Fig.(a) and (d) presents the *I-V* curve and the fitting for 1L-MoS_2 and 2L-MoS_2 samples, respectively. The square presents the current voltage *(I-V)* curve obtained by CAFM measurements. The reverse bias region is fit by a thermionic emission model (red line) while the forward bias region is fit by a Fowler-Nordheim (FN) tunneling model (blue line). Fig.(b) and (e) present the linear behavior of $ln\frac{1}{V^2}$ -$1/V$ plot in the forward bias regime, which suggests that the current is due to FN tunneling. Fig.(c) and Fig.(f) present the plot $ln\frac{1}{V^2}$ -$1/V$ in the reverse bias regime. The inset of the plots Fig.(c) and Fig.(f) are showing the linear behavior of the $ln\, I - V$ plot, which suggests that the current is due to thermionic emission.

In the reverse bias regime, we use thermionic emission model to model our *I-V* behavior, which was also used before in explaining the charge transport through MoS_2 layers.[3, 7] The current due to thermionic emission model[1] is given by

$$I = I_0\left[e^{\frac{qV}{\eta k_B T}} - 1\right] \qquad (2)$$

where η is known as the ideality factor and I_o is called the saturation current, which is given by

$$I_0 = A_e A^* T^2 e^{-\frac{q\Phi_B}{k_B T}} \qquad (3)$$

Here A_e denotes the effective contact area. Eq.(2) suggests that $\ln I$ will vary linearly as a function of the voltage due to the thermionic equation. Indeed, we have observed a linear behavior in the $\ln I$ vs V plot as shown in the inset of Fig.S6(c) and Fig.S6(f) for 1L-MoS_2 and 2L-MoS_2, respectively. This confirms that the current in the reverse bias is due to thermionic emission.

S6: MoS_2 on rough thermally grown Au and commercially available ITO

We have also studied few-layers MoS_2 exfoliated on thermally grown rough Au substrate and commercially available ITO. The height profile and the current mapping of a monolayer MoS_2 sample on rough Au surface are shown in Fig.7(a-b) and Fig.7c, respectively. We note that the height profile of the sample varies over several nanometers. Local height variations will introduce straining effect and may modify the transport measurements.[8, 9] The height profile of MoS2 sample on a commercially available ITO substrate is shown in Fig.7(d).

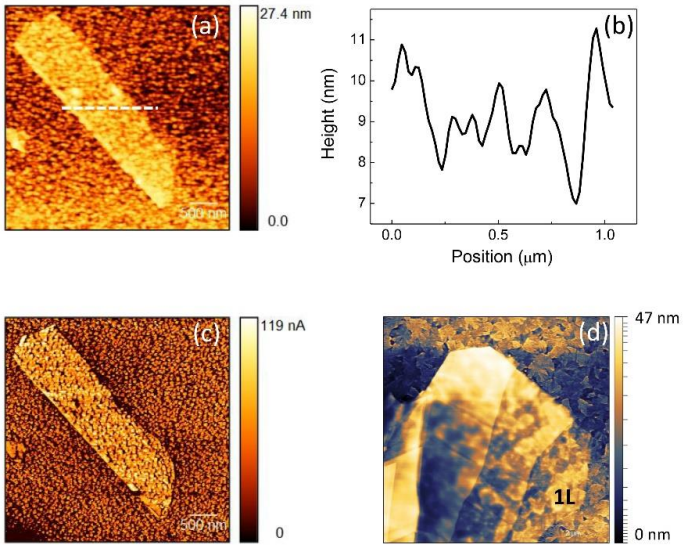

Figure S7: MoS_2 samples on rough substrate. (a) Height profile AFM measurement of a monolayer MoS_2 sample on thermally grown Au substrate. (b) Height profile along the white dashed line in Fig.(a). (c) The spatial current mapping of the sample presented in Fig.1(a). (d) The height profile of the a few layer MoS_2 sample on a commercially available ITO substrate.

S7. Electronic transport along the edges

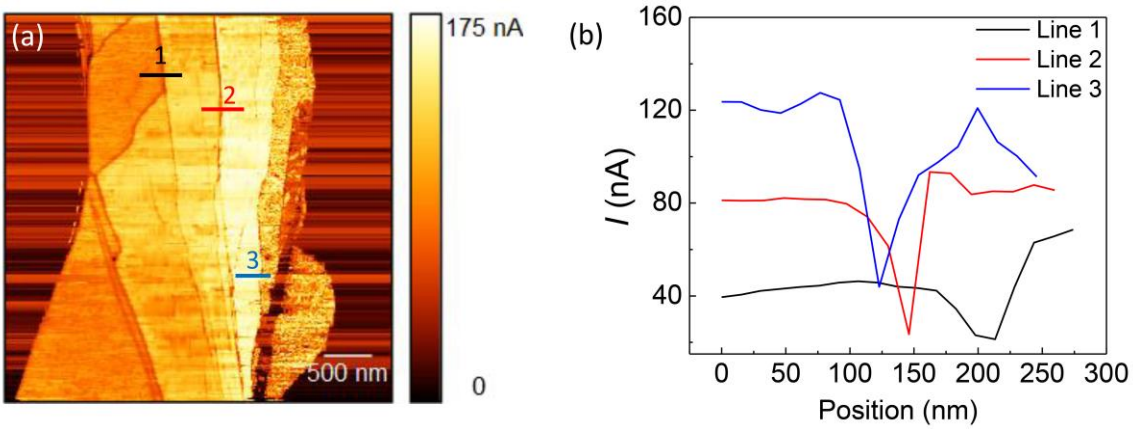

Figure S8: (a) Left is presenting the current map of MoS_2 sample on an ITO substrate. The current is measured at 1.3 V. Three lines of different (black, red and blue) are marked whose current profiles are presented in Fig. (b).

S8. Work function calculations

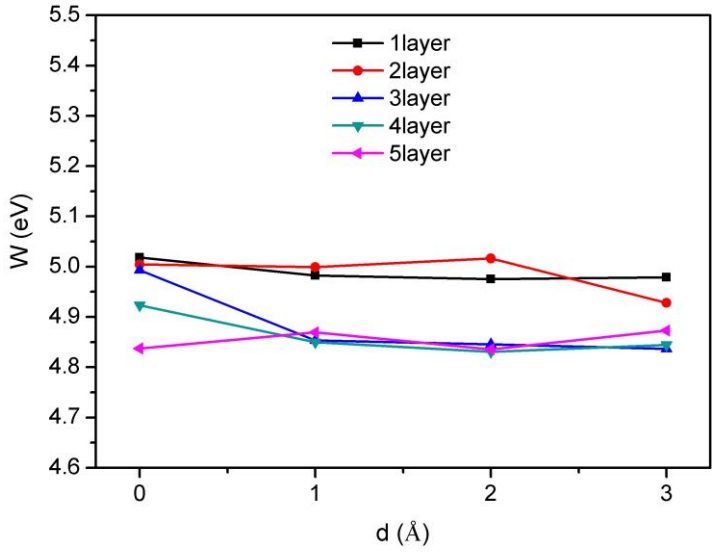

Figure S9. Calculated work function of MoS_2 on Au as a function of the thickness of MoS_2 and the interfacial spacing between the first layer of MoS_2 and the Au (111) surface. This work function has been used to calculate the Schottky barrier in Figure 4c in the main text.

S9: Photoconductive AFM measurements setup

The experimental setup of the photoconductive AFM measurements is shown in Fig.S9.

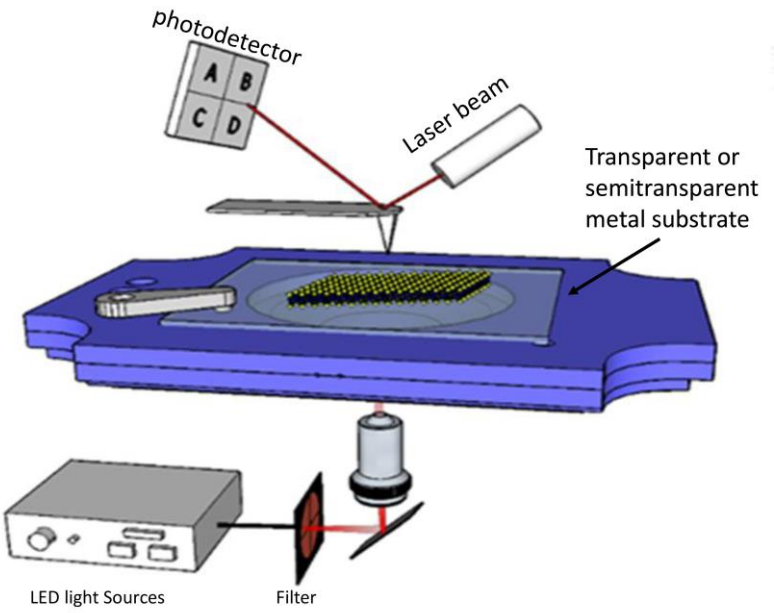

Figure S9: Photoconductive AFM measurements. Filters were used to select the color of the excitation light. Few-layer MoS_2 samples were prepared on transparent or semitransparent substrate to ensure high light transmission.

S10: Negative photoconductivity of few layer MoS_2 on different metal surfaces

We studied the negative photoconductivity of few layer MoS_2 samples on rough Ito surfaces and template stripped Au surfaces. The results is shown in figure S10.

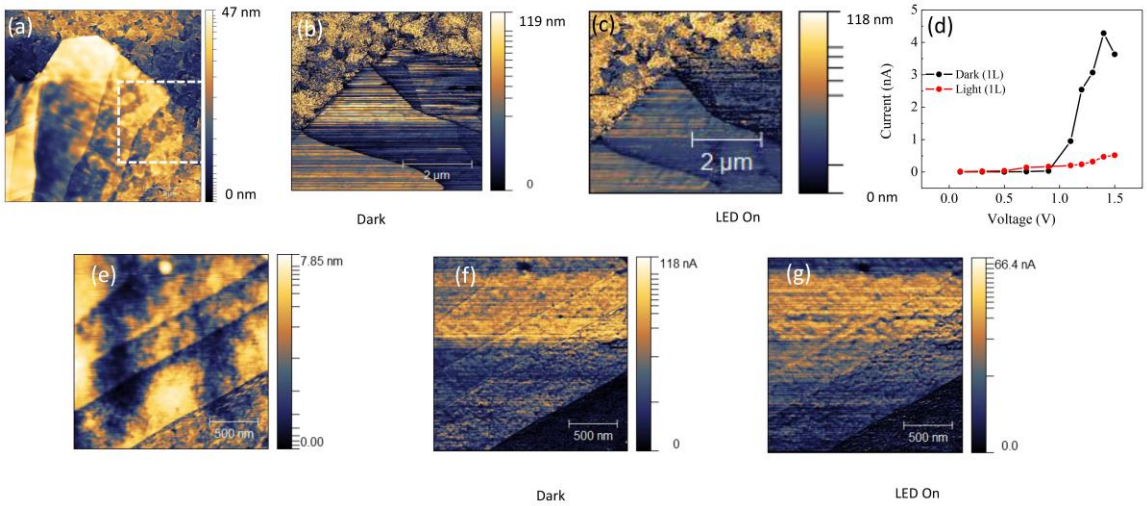

Figure S10: Negative photoconductivity of few layer MoS_2 on commercially available rough ITO surface (Fig.a-d) and template stripped Au-surfaces (Fig.e-g). Fig(a) presents the surface profile of the ITO surface. CAFM measurements of few layer MoS_2 sample with light and without light are presented in Fig.(b) and Fig.(c), respectively. The data were recorded for samples under bias 1.5V. Voltage dependence current data is presented in Fig.(d). (e) The height profile AFM image of a MoS_2 sample directly exfoliated on a template stripped Au surface. To ensure light transmission, the template stripped Au substrate was prepared on a glass substrate.

References:

1. Sze, S. M.; Ng, K. K. *Physics of Semiconductor Devices*. 3rd ed.; Wiley-Interscience: Hoboken, N.J., 2007; p 712
2. Rhoderick, E. H. Metal-Semiconductor Contacts. *IEE Proceedings I - Solid-State and Electron Devices* **1982**, 129, 1.
3. Son, Y.; Wang, Q. H.; Paulson, J. A.; Shih, C.-J.; Rajan, A. G.; Tvrdy, K.; Kim, S.; Alfeeli, B.; Braatz, R. D.; Strano, M. S. Layer Number Dependence of MoS_2 Photoconductivity Using Photocurrent Spectral Atomic Force Microscopic Imaging. *ACS Nano* **2015**, 9, 2843-2855.
4. Ahmed, F.; Choi, M. S.; Liu, X.; Yoo, W. J. Carrier Transport at the Metal–Mos2 Interface. *Nanoscale* **2015**, 7, 9222-9228.
5. Hattori, Y.; Taniguchi, T.; Watanabe, K.; Nagashio, K. Determination of Carrier Polarity in Fowler–Nordheim Tunneling and Evidence of Fermi Level Pinning at the Hexagonal Boron Nitride/Metal Interface. *ACS Applied Materials & Interfaces* **2018**, 10, 11732-11738.
6. Lee, S.; Choi, K. Y.; Lee, S.; Park, B. H.; Park, J. G. Tunneling Transport of Mono- and Few-Layers Magnetic Van Der Waals Mnps3. *Apl Mater* **2016**, 4.
7. Li, Y.; Xu, C.-Y.; Zhen, L. Surface Potential and Interlayer Screening Effects of Few-Layer Mos2 Nanoflakes. *Appl. Phys. Lett.* **2013**, 102, 143110.
8. Conley, H. J.; Wang, B.; Ziegler, J. I.; Haglund, R. F.; Pantelides, S. T.; Bolotin, K. I. Bandgap Engineering of Strained Monolayer and Bilayer Mos2. *Nano Lett.* **2013**, 13, 3626-3630.
9. English, C. D.; Shine, G.; Dorgan, V. E.; Saraswat, K. C.; Pop, E. Improved Contacts to Mos2 Transistors by Ultra-High Vacuum Metal Deposition. *Nano Lett.* **2016**, 16, 3824-3830.